Robust Control Design for Ride-Through/Trip of Transformerless Onboard Bidirectional EV Charger with Variable-Frequency Critical-Soft-Switching

Liwei Zhou, *Student Member, IEEE*, Matthew Jahnes, *Student Member, IEEE*, Matthias Preindl, *Senior Member, IEEE*

***Abstract*—A transformerless electric vehicle (EV) onboard charger is designed for robust grid fault ride-through/trip capabilities and the attenuation of leakage current (<20mA) with high efficiency. A zero sequence voltage control method is developed with a modified grid-connected LCL inverter to stabilize the zero-sequence voltage and bypass the leakage current. The topological modification is configured by connecting the common points of three-phase output capacitors and the positive/negative DC bus terminals. The control strategies include (1) AC grid side: dq sequence grid side current control, q sequence reactive power control and zero-sequence grid voltage/switch side inductor current control; (2) DC battery side: constant current (CC) and constant voltage (CV) control. An optimal control parameter design procedure is developed based on active damping method to improve the dynamic performance and attenuate the LCL filter resonance for a better grid disturbance response. The developed onboard charger is capable of dealing with abnormal grid voltage/frequency conditions to properly ride through and trip based on the standard requirements of IEEE Std. 1547. Also, the onboard charger can be applied to the integrated drivetrain. An AC current mode variable-frequency critical-soft-switching (VF-CSS) technique is developed for the onboard charger to achieve high efficiency (>99%). The performance under abnormal grid conditions are tested experimentally to verify the ride-through and trip capabilities of the developed onboard charger in compliance with IEEE Std. 1547. Also, the experiments have validated the low leakage current, stable zero sequence voltage and full range of variable-frequency soft-switching for high efficiency.**

***Index Terms*—Transformerless onboard charger, variable-frequency critical-soft-switching control, LCL filter, zero-sequence voltage control, active damping method, grid fault ride-through/trip.**

I. Introduction

ELECTRIC vehicle (EV) charger is playing a significant role in the popularization of electrified transportation system. Based on whether the AC power interface location is inside or outside the EV, the charger can be classified as AC and DC charger [1]. For the DC charger, a stationary off-board charger enclosure is needed with converter inside to deliver power from AC grid to the DC battery. The DC charger is typically bulky and fast. For the AC charger, the converter is integrated inside the car with limited space. Thus, it is not easy to increase the AC charging power to a high level [2], [3]. Also, from a standard requirement perspective, leakage current should be maintained within a low level for safety issue. Typically, a transformer is needed to block the leakage current from flowing to the grid and EV chassis which brings extra power losses and consumes more space [4], [5]. Another important topic is that the long charging time for onboard charger requires more robust control method to be interfaced with the grid especially during abnormal grid conditions [6], [7]. This paper focuses on the onboard AC charger integrated into the drivetrain system with the issues of leakage current, power losses and robust grid interface of ride-through/trip during long charging time.

Firstly, for the onboard charger, the leakage current is one of the most critical issues that affects the personal safety [8], [9]. Conventionally, the isolated AC/DC converter is configured as the onboard charger with a high frequency transformer to block the leakage current as is shown in Fig. 1. However, the high frequency transformer is typically inserted in the DC/DC conversion stage which will be split into DC/AC+AC/DC stages [10]. Thus, compared to the non-isolated topology, an extra power conversion stage and a transformer are added. The power losses, volume and cost will be increased accordingly [11], [12]. Different from the two-stage isolated converter in Fig. 1 and the conventional transformerless three-phase LCL inverter in Fig. 2, this paper developed a modified non-isolated single stage onboard charger to attenuate the leakage current without using transformer or extra power stages. The power losses, volume and cost will be largely reduced [13]. The modified topology is shown in Fig. 3 [14] which consumes the same number of switches and 3 more output upper capacitors compared with Fig. 2. Although the number of output capacitors are increased, the total capacitance are kept the same which means, instead of 3 larger capacitors, the modified topology is configured with 6 smaller capacitors. Thus, the total volume of the output capacitors for the modified topology is similar with the conventional one.

Secondly, for the improvement of efficiency, the soft switching technique can be applied to reduce the switching losses of the power converter [15]. For the soft switching techniques, the main idea is to reduce the overlap between the voltage and current across the switches during turn-on and turn-off transients [16]. Several topological modifications have been proposed to implement the soft switching which can be summarized as zero voltage switching (ZVS) and zero current switching (ZCS) [17], [18]. From the control perspective to implement soft switching without extra circuit changes, the large turn-on losses can be replaced with small turn-off losses with a variable-frequency critical-soft-switching (VF-CSS) technique that is developed in this paper for the onboard charger [19],

[20].

Thirdly, for the grid interfacd ride-through/trip, since the onboard charger is directly plugged to the AC grid from the car and the charging period is typically several hours, the possibilities of encountering abnormal grid voltage/frequency conditions are higher than the DC fast charging [21]. The average EV has a battery capacity of around 36 kWH, and average onboard power rating of 6.6kW, taking around 5.5 hours to charge the EV from empty to full, with the average Level 2 charger. Thus, it is necessary to develop the onboard charger with robust grid fault ride-through/trip capabilities [22], [23].

Fourthly, an overall state of the art for the EV onboard charger and the ride through/trip robustness is introduced. Several EV onboard chargers are designed to improve the performances in the aspects of efficiency, power density, grid services, power quality and level of integration [24]–[34]. Specifically, [24] studied the transient performance to achieve zero-voltage switching by applying GaN and Si modules. [25] and [26] developed the resonance circuit design techniques to improve the efficiency and reliability of EV chargers. For the grid services application on EV chargers, [27], [28], [30] designed Vehicle-to-Grid (V2G) functions to provide grid voltage regulations with reactive power compensation. [29] proposed operation procedures for the electric-drive-reconstructed onboard charger when faults occurred on the motor. However, grid faults operations and control robustness studies for EV chargers lack detailed research. Also, the power quality of onboard charger is improved by reducing the current ripple in [31]. For the integration of charger and motor system, [32]–[34] proposed different circuitry structures to achieve multi-functions for low cost by reusing the shared components between the charger and motor circuits. [32] reused the charging circuits for both propulsion battery and auxiliary low voltage battery while providing grid services on a single-phase application. [33] studied an EV onboard charger system integrated into six-phase machine by directly connecting the three-phase grid to the middle point of machine's phase winding. [34] leveraged the traction inverter phase legs for both charging and driving modes to reduce cost in a six-phase machine system.

This paper develops a transformerless onboard EV charger integrated into the drivetrain system with zero sequence voltage stabilized control method, AC current mode full range variable-frequency critical-soft-switching and robust grid fault ride-through/trip capabilities. Firstly, the topological modeling and control strategies of the developed transformerless onboard charger is analyzed in $dq0$ reference frame to attenuate the leakage current with a zero sequence voltage stabilization instead of high frequency transformer. Secondly, The variable-frequency critical-soft-switching technique is applied to maintain soft switching operation during the whole line period and improve the efficiency to above 99%. Thirdly, an optimal control parameter tuning method and grid fault ride-through/trip control procedure are designed, respectively, in compliance with IEEE Std. 1547 [35]. For a better grid disturbance response, an active damping method is developed with the tuning strategies of active damping factor and control gain. The developed transformerless onboard charger is validated experimentally.

The contributions of this paper can be summarized in three aspects. (1) A robust control parameter design method to improve the stability and dynamic performance of EV onboard charger under grid abnormal conditions without being influenced by the uncertainties from grid side. (2) A modified three-phase inverter by connecting the output upper/lower capacitors to the positive/negative DC bus terminals to bypass the leakage current from flowing into the grid with a zero-sequence voltage control method; (3) A variable-frequency critical-soft-switching method to be applied on the modified transformerless EV onboard charger for the improvement of efficiency by 2%. The combination of variable frequency control with a grid connected onboard charger application may cause some stability issue due to a time-varying switching frequency. The proposed robust control parameter design method can solve this transient oscillation by deriving the optimal control gain and active damping factor.

II. Grid Abnormal Condition Requirements

The grid abnormal conditions mainly include voltage/frequency fluctuations and deviations away from the rated values. IEEE Std. 1547 [35] defines the specific requirements for the distributed energy resources (DER) integrated into the grid to respond when grid faults occur. Onboard EV chargers have more chances to encounter grid abnormal conditions compared with the DC fast charger since the charging time is longer. Thus, the ride-through and trip design for onboard EV charger is essential. The IEEE Std. 1547 for grid abnormal condition requirements are illustrated in this section.

A. Grid Voltage Abnormal Condition Requirements

IEEE Std. 1547 regulates the ride-through and trip requirements under different grid voltage fluctuation ranges. V_g and V_N are the measured and rated grid voltages, respectively. Firstly, when $90\%V_N < V_g < 110\%V_N$, the charger should stay connected and be operating. Secondly, if $110\%V_N < V_g < 120\%V_N$, $65\%V_N < V_g < 90\%V_N$ or $30\%V_N < V_g < 65\%V_N$, the charger should be able to ride through for 1s, 2s or 0.32s and then trip. Lastly, if $V_g > 120\%V_N$ or $V_g < 30\%V_N$, the charger could trip immediately.

B. Grid frequency Abnormal Condition Requirements

IEEE Std. 1547 also regulates the trip requirements under different grid frequency fluctuation ranges. f_{grid} and f_N are the measured grid frequency through PLL and rated grid frequency, respectively. With a rated line frequency of 50Hz, if $f_N - 3Hz < f_{grid} < f_N + 1.8Hz$, the charger is required for a mandatory operation. If $f_{grid} > f_N + 1.8Hz$ or $f_{grid} < f_N - 3Hz$, the charger could trip immediately.

III. Modeling and Control

The topology, modeling and control strategies of the developed transformerless onboard EV charger are shown in this section.

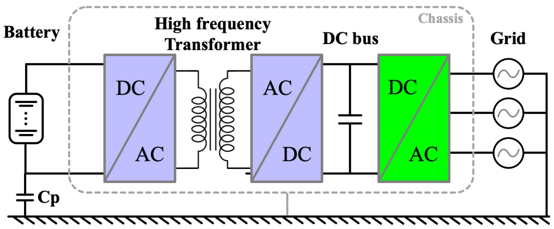

Fig. 1. Conventional isolated EV charger with high frequency transformer.

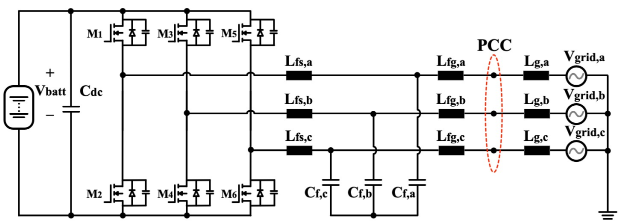

Fig. 2. Conventional transformerless three-phase grid-connected LCL inverter .

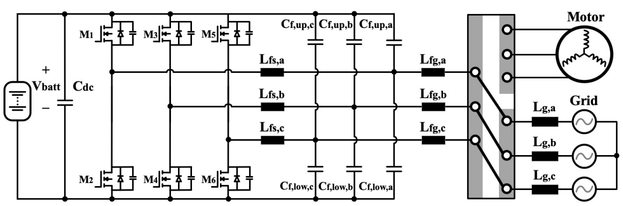

Fig. 3. Developed transformerless onboard EV charger integrated in the drivetrain system with low leakage current.

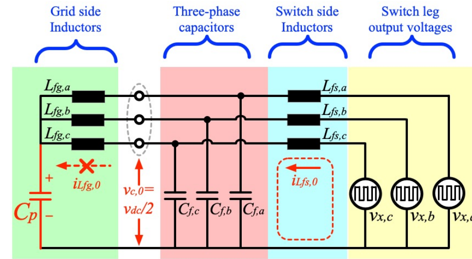

(a) Equivalent overall CM circuit.

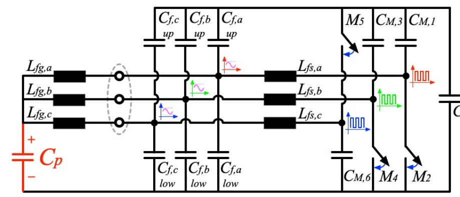

(b) CM circuit in active state.

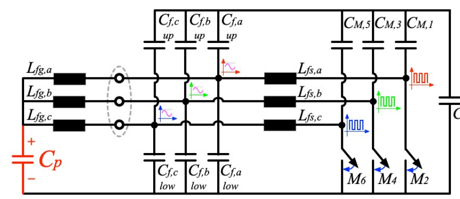

(c) CM circuit in null state.

Fig. 4. The equivalent CM circuit (a) overall (b) in active state (c) in null state.

A. Non-isolated Topology

The topology of the transformerless EV onboard charger is shown in Fig. 3. Different from the traditional LCL inverter in Fig. 2, the modified topology connects the common points of the three-phase output capacitors and the positive/negative DC bus terminals. This topological modification is aimed at stabilizing the zero-sequence voltage and attenuating the leakage current on grid side with the help of zero-sequence voltage/current controller.

The definition of common mode voltage and leakage current are defined as:

$$i_{leakage} = \frac{dv_{cm}}{dt} = \frac{d(v_a + v_b + v_c)/3}{dt}. \tag{1}$$

Since the leakage current is proportional to the rate of change of the common mode voltage, the developed transformerless onboard charger is designed to maintain a constant zero-sequence grid voltage with the help the topological modification in Fig. 3. As is shown in Fig. 4(a) of the equivalent common mode circuit for the modified topology, the three-phase output capacitor star points are connected to the DC bus terminals. Thus, the leakage current path generated by the switching leg high frequency pulse voltages will be bypassed by the modified connections with the zero-sequence grid voltage control. The leakage current will only circulate within the switch side LC filter paths instead of flowing into the grid.

B. Common Mode Analysis

The detailed common mode analysis of the modified converter is illustrated in this section. The equivalent common mode (CM) circuits in the active and null states are shown in Fig. 4(b) and 4(c), respectively. Taking the active state of Fig. 4(b) for example, the lower switches, M_2 and M_4, and upper switch, M_5, are turned on. The other switches are turned off with the corresponding equivalent switch capacitors, $C_{M,1}$, $C_{M,3}$ and $C_{M,6}$, in the CM circuit. On the other hand, in the null state of Fig. 4(c), all the lower switches, M_2, M_4 and M_6, are turned on. The upper switches are turned off with the corresponding equivalent switch capacitors, $C_{M,1}$, $C_{M,3}$ and $C_{M,5}$, in the CM circuit. As indicated in the CM circuit, the phase leg output voltages are high frequency pulsations. However, with the filtering components of upper/lower output capacitors, $C_{f,abc,up}$ and $C_{f,abc,low}$, and switch side inductors, $L_{fs,abc}$, the high frequency voltage pulsations can be filtered into low frequency sinusoidal waveforms.

For the transient analysis of the CM circuit, during the active switching state in Fig. 4(b), the three-phase output capacitor voltages can be approximated as:

$$v_{Cf,a,active} = \frac{C_{f,a,low}}{(C_{f,a,up} + C_{M,1}) + C_{f,a,low}} V_{dc} \quad (2a)$$

$$v_{Cf,b,active} = \frac{C_{f,b,low}}{(C_{f,b,up} + C_{M,3}) + C_{f,b,low}} V_{dc} \quad (2b)$$

$$v_{Cf,c,active} = \frac{C_{f,c,low} + C_{M,6}}{C_{f,c,up} + (C_{f,c,low} + C_{M,6})} V_{dc}. \quad (2c)$$

During the null switching state in Fig. 4(c), the three-phase output capacitor voltages can be approximated as:

$$v_{Cf,a,null} = \frac{C_{f,a,low}}{(C_{f,a,up} + C_{M,1}) + C_{f,a,low}} V_{dc} \quad (3a)$$

$$v_{Cf,b,null} = \frac{C_{f,b,low}}{(C_{f,b,up} + C_{M,3}) + C_{f,b,low}} V_{dc} \quad (3b)$$

$$v_{Cf,c,null} = \frac{C_{f,c,low}}{(C_{f,c,up} + C_{M,5}) + C_{f,c,low}} V_{dc}. \quad (3c)$$

Thus, either in the active state or null state, the output upper and lower capacitors smoothen the output common mode voltage to be closer to V_{dc}/2 based on the voltage evenly splitting function of $C_{f,abc,up}$ and $C_{f,abc,low}$. The influence of switch capacitors in (2) and (3) on the voltage evenly splitting can be attenuated by the zero sequence voltage control to adjust the switching PWM modulation.

C. System Modeling

The LCL filtered DC/AC converter is controlled in $dq0$ reference frame mainly for two considerations: (1) DC reference tracking is easier to be implemented with PI controller; (2) The zero-sequence grid voltage/inductor current can be extracted in $dq0$ reference frame for a direct control. With the help of Clarke and Park transformations, the modeling of the LCL converter can be converted from abc reference frame to $dq0$ system as:

$$\dot{i}_{L,dq0} = \frac{1}{L_f}\mathbf{I}u_{x,dq0} - \frac{1}{L_f}\mathbf{I}u_{c,dq0} - \omega\mathbf{G}i_{L,dq0} \quad (4a)$$

$$\dot{u}_{c,dq0} = \frac{1}{C_f}\mathbf{I}i_{L,dq0} - \frac{1}{C_f}\mathbf{I}i_{g,dq0} - \omega\mathbf{G}u_{c,dq0} \quad (4b)$$

$$\dot{i}_{g,dq0} = \frac{1}{L_g}\mathbf{I}u_{c,dq0} - \frac{1}{L_g}\mathbf{I}u_{g,dq0} - \omega\mathbf{G}i_{g,dq0} \quad (4c)$$

where $u_{x,dq0}$, $i_{L,dq0}$, $u_{c,dq0}$, $i_{g,dq0}$, $u_{g,dq0}$ are the switch leg output voltage, switch side inductor current, output capacitor voltage, grid side inductor current and grid voltage, respectively. ω is the grid angular velocity in rad/s. $\mathbf{I}$ is the 3×3 identity matrix. $\mathbf{G}$ is the coupling term matrix caused by the transformations and is expressed as [0, -1, 0; 1, 0, 0; 0, 0, 0]. The derived dq0 system state space equations can be applied to extract the zero sequence voltage/current. Thus, based on the connection between three-phase capacitors common points and positive/negative DC bus terminals, the zero sequence voltage can be stabilized and the leakage current on grid side can be bypassed with the developed design strategies.

D. Control

The control diagram of the developed transformerless onboard EV charger is shown in Fig. 5 which includes (1) AC grid side: dq-sequence grid current control, q-sequence reactive power control and zero-sequence grid voltage/inductor current control; (2) DC battery side: constant current (CC) and constant voltage (CV) control. (3) Phase-locked-loop control.

1) AC side control: The d-axis grid current component is controlled by receiving the reference from preceding stage of DC side CC/CV controller output for active power control. The q-axis grid current component is controlled by receiving the reference from preceding stage of reactive power controller. With the connections of three-phase output capacitors common points and the positive/negative DC bus terminals, the zero-sequence switch side inductor current is independently controlled by receiving the reference from preceding stage of zero-sequence grid voltage controller. The zero-sequence grid voltage controller is designed to maintain the common mode voltage as a constant of half DC bus voltage, $Vdc/2$. Thus, the zero-sequence voltage can be stabilized with less fluctuation. Based on the calculation of grid leakage current: $i_{leakage} = C_p du_{cm}/dt$, the zero-sequence grid current can be attenuated with the stabilization of zero-sequence voltage.

2) DC side control: The cascaded constant current (CC) and constant voltage (CV) controllers are designed for the DC battery side. The upper/lower limits for the CV controller output are configured to achieve the rated charging/discharging current. The CC controller passes the battery current reference to the latter stage of d-axis grid current controller.

3) Phase-locked-loop: The transformations between abc and $dq0$ needs the real-time phase angle information, θ, of the grid voltage. An effective way can be implemented with a PI controller by controlling the q component of the grid voltage, $v_{g,q}$, to be zero to derive the angular velocity, ω, of the phase angle. The phase-locked-loop (PLL) control are also applied to check the real time grid frequency for the detection of grid frequency abnormal conditions to ride-through/trip.

E. Variable-Frequency Critical-Soft-Switching (VF-CSS)

The soft switching technique, VF-CSS, is developed in the full AC period with variable switching frequency to substitute the high turn-on losses of the upper switch with low turn-off losses of the lower switch [36], [37]. The principle of implementing VF-CSS is to keep the peak/valley points of the switch side inductor current, i_L, larger/smaller than the threshold current value, I_{th} and $-I_{th}$, respectively. The VF-CSS operation diagram is shown in Fig. 6 where the upper and lower switch signals and the corresponding inductor current waveforms are presented. In general, the VF-CSS is designed to tune the switching frequency, f_{sw}, by following the equation below:

$$f_{sw} = \frac{(1-d)dv_{dc}}{2(|i_L| + I_{th})L_{fs}}, \quad (5)$$

where I_{th} is the boundary threshold current for soft switching which could be derived with a given dead time and switch output capacitance. The efficiency of the transformerless onboard EV charger is improved to be above 99% with the VF-CSS.

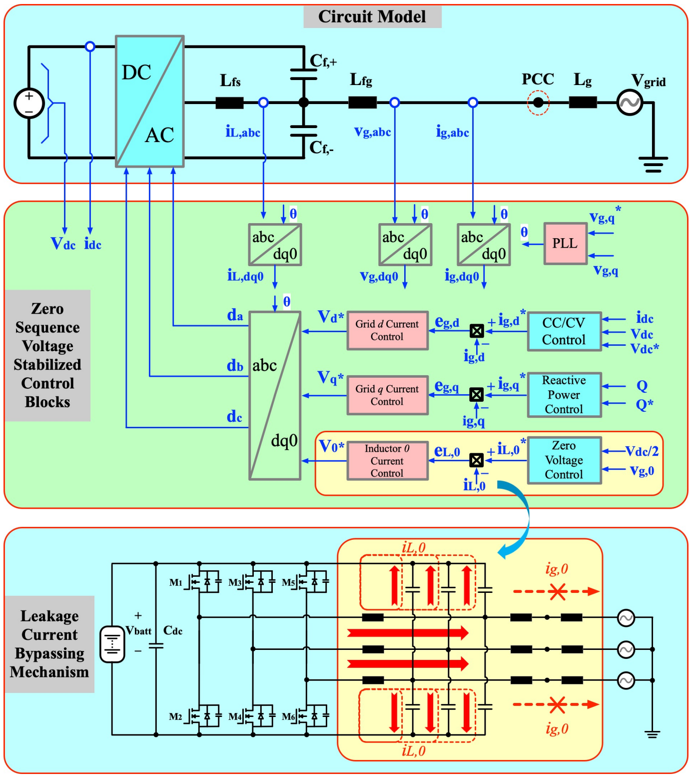

Fig. 5. Developed control diagram of the transformerless integrated onboard EV charger with zero sequence voltage stabilization.

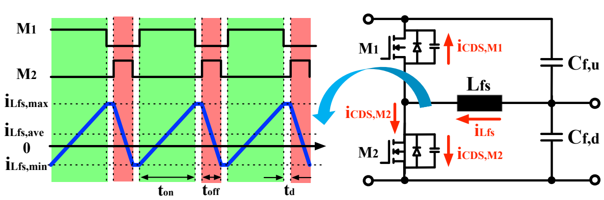

(a) Critical soft switching technique.

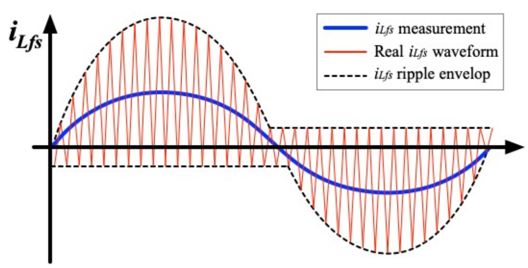

(b) AC current mode application.

Fig. 6. (a) The critical soft switching technique for one phase module and (b) the AC current mode application.

IV. Control Parameters and Grid Fault Ride-Through/Trip Design

The ride-through and trip design of the developed transformerless onboard EV charger under grid voltage/frequency abnormal conditions are analyzed in this section. The charger is compliant with IEEE Std. 1547 standard requirements for the contribution of grid stability [38], [39].

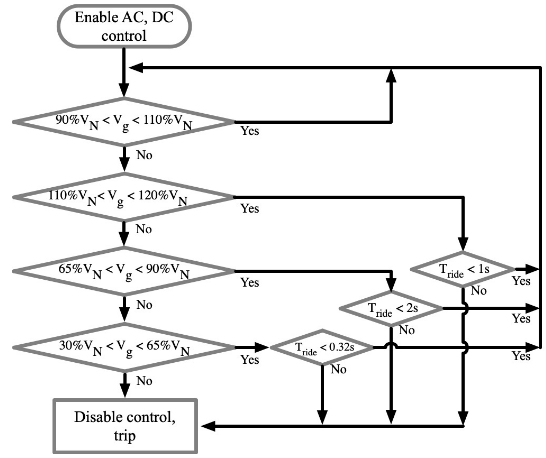

(a) Grid voltage ride-through/trip design.

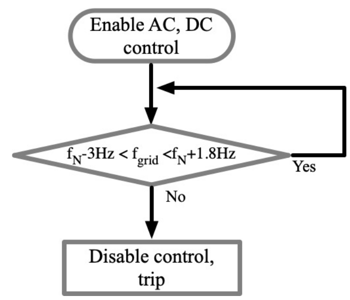

(b) Grid frequency trip design.

Fig. 7. Flow chart of the (a) grid voltage and (b) grid frequency abnormal conditions ride-through/trip design.

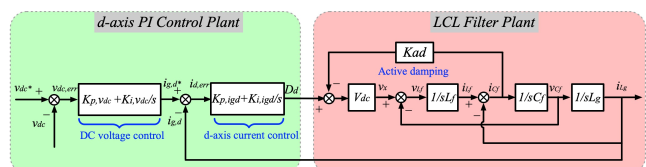

(a) d-axis control plant model.

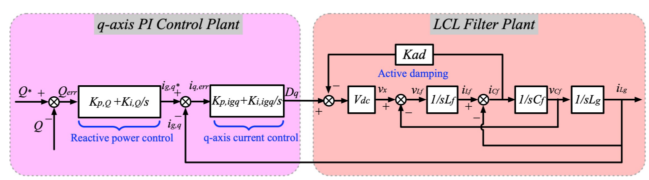

(b) q-axis control plant model.

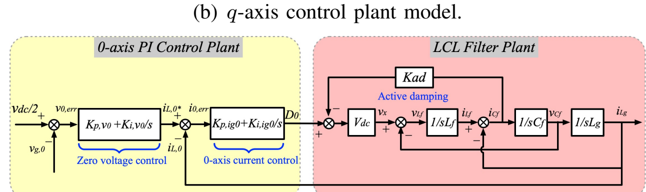

(c) 0-axis control plant model.

Fig. 8. Control plant models in (a) d-axis, (b) q-axis and (c) 0-axis.

A. Grid Voltage Faults Ride Through/Trip Deisgn

Fig. 7(a) shows the flow chart of the grid voltage abnormal conditions ride-through/trip design. In every control period, the d-sequence of grid voltage is checked for the detection of grid voltage amplitude. T_{ride} represents the ride-through time. If the grid voltage amplitude is fluctuating within the specific voltage ranges, the time counter for T_{ride} will start ride-through timekeeping and check if T_{ride} exceeds the maximum requirement. If the grid voltage recovers to normal condition within maximum ride-through time, T_{ride} will be reset. Otherwise, the charger will trip.

B. Grid Frequency Faults Ride Through/Trip Design

Fig. 7(b) shows the flow chart of the grid frequency abnormal conditions trip design. Fig. 7(b) shows the flow chart of the grid frequency abnormal conditions trip design. In every control period, the angular velocity of the grid, ω, is checked for the detection of grid frequency based on the PLL controller. If the grid frequency exceeds the required mandatory operating range, the charger will trip. Otherwise, the charger will be kept operation.

C. Robust Control Design for Grid Disturbance

To achieve a fast and robust dynamic performance for grid fault ride-through/trip and solve the resonance oscillation issue, the control parameters are designed and optimized with an active damping method applied to the LCL filtered converter controller. The control gain and damping factor are adjusted to optimize the rising time and overshoot for the improvement of grid abnormal condition transient performance. A design flowchart is proposed for the parameter tuning.

Fig. 8 shows the active damping control plant models of the developed transformerless onboard EV charger in d, q and zero reference frames, respectively. The control plant model includes the former stage of PI control plant and latter stage of LCL filter plant.

In an LCL filter system, the resonance frequency is calculated as:

$$\omega_{res} = \sqrt{\frac{L_{sf}+L_{gf}}{L_{sf}L_{gf}C_f}}. \tag{6}$$

The transfer function on the left side of the LCL filter plant model from the input of duty cycle to the output of grid current without active/passive damping can be derived as

$$G_{LCL}(s) = \frac{I_g(s)}{D(s)} = \frac{v_{dc}}{L_{sf}L_{gf}C_f s^3 + (L_{sf}+L_{gf})s}. \tag{7}$$

As is shown in Fig. 8, to eliminate the resonance frequency spikes, the active damping term can be extracted from the capacitor current and multiplied by an active damping gain, K_{ad}, then fed back to the duty cycle. The transfer function of active damping LCL filter can be derived as

$$G_{LCL,ad}(s) = \frac{I_g(s)}{D(s)} = \frac{v_{dc}}{L_{sf}L_{gf}C_f s^3 + v_{dc}K_{ad}L_{gf}C_f s^2 + (L_{sf}+L_{gf})s}. \tag{8}$$

Thus, with the help of the introduced active damping gain, K_{ad}, an extra term of s^2 is added to the denominator of the transfer function for the improvement of LCL filter system stability. Doing so, the resonance can be attenuated and the control gains can be further increased to expand the control bandwidth.

Equation (8) can be rewritten as the format of damped model of

$$G_{LCL,ad}(s) = \frac{v_{dc}}{L_{gf}L_{sf}C_f s(s^2 + 2\zeta\omega_{res}s + \omega_{res}^2)} \tag{9}$$

where ζ and ω_{res} represent the active damping factor and resonant frequency, respectively. ω_{res} is determined by the LCL passive filter values and has been derived in equation (6). Thus, to compare the equations (8) and (9) of the denominators, the active damping gain, K_{ad}, can be expressed by the LCL filter values and active damping factor, ζ,

$$K_{ad} = \frac{4\zeta}{v_{dc}}\sqrt{\frac{L_{fs}(L_{fs}+L_{fg})}{L_{fg}C_f}}. \tag{10}$$

Since, for a typical second order system, the active damping factor of LCL is usually designed as 0.707, the active damping gain can be derived accordingly for the initialization of control parameter design flowchart.

Based on the control and LCL filter plant models in Fig. 8, the active damping open loop control transfer functions from grid/switch side inductor current tracking error, i_{err}, to the measurements, i_g, of grid current can be expressed in $dq0$ as:

$$G_{igderr2ig,ad}(s) = (K_{p,igd} + \frac{K_{i,igd}}{s})G_{LCL,ad}(s) \tag{11a}$$

$$G_{igqerr2ig,ad}(s) = (K_{p,igq} + \frac{K_{i,igq}}{s})G_{LCL,ad}(s) \tag{11b}$$

$$G_{iL0err2ig,ad}(s) = (K_{p,ig0} + \frac{K_{i,ig0}}{s})G_{LCL,ad}(s). \tag{11c}$$

Then, by adding the outer loop DC bus, reactive power and zero-sequence voltage controllers, the whole system of active damping open loop control transfer function in Fig. 8 can be expressed as:

$$G_{d,vdc2ig,ad}(s) = (K_{p,vdc} + \frac{K_{i,vdc}}{s})\frac{G_{igderr2ig,ad}(s)}{1+G_{igderr2ig,ad}(s)} \tag{12a}$$

$$G_{q,Q2ig,ad}(s) = (K_{p,Q} + \frac{K_{i,Q}}{s})\frac{G_{igqerr2ig,ad}(s)}{1+G_{igqerr2ig,ad}(s)} \tag{12b}$$

$$G_{0,v02iL,ad}(s) = (K_{p,v0} + \frac{K_{i,v0}}{s})\frac{G_{iL0err2ig,ad}(s)}{1+G_{iL0err2ig,ad}(s)}. \tag{12c}$$

Since the inner loop of dq grid current and zero sequence inductor current controllers are the blocks to be directly interfaced with the duty cycles which significantly determine the control bandwidth, the current control gains are critical to be fine tuned. The initial values for optimal PI gains design of the LCL filtered converter can follow the equations below [40]:

$$K_{p,ig} = \frac{(L_{fs} + L_{fg})f_{sw}}{3} \tag{13a}$$

$$\tau_{i,ig} = \frac{L_{fs} + L_{fg}}{R_{fs} + R_{fg}} \tag{13b}$$

where f_{sw} and $\tau_{i,ig}$ are the switching frequency and integral time constant, respectively. For the initial value of switching frequency, a lower limit value can be chosen as the starting point based on the lower boundary condition of critical soft switching operation in equation (5).

For a robust grid fault ride-through and trip capabilities, the developed transformerless onboard EV charger needs a fast and robust controller to minimize the rising time and overshoot during the transient period. A control parameter design flowchart is proposed in Fig. 9. Firstly, the active damping gain, K_{ad}, and control gain of the inner loop current controller, K_p, are initialized based on (10) and (13). Secondly, K_{ad} is iterated with a step of ΔK_{ad} to derive the open and closed loop current control transfer function. Thirdly, the step response of the closed loop transfer function is plotted as is shown in Fig. 10(a). The rising time and overshoot values are evaluated with the first checking conditions in the flowchart. When the overshoot is larger than 5% or the rising time is within 5ms, the iteration of K_{ad} will be stopped with a relatively fast control (5ms) and low overshoot (5%). Then, fourthly, the current control gain, K_p, is iterated with a step of ΔK_p to derive the open and closed loop current control transfer function. Fifthly, the step response of the closed loop transfer function is plotted as is shown in Fig. 10(b). The rising time and overshoot values are further evaluated with the second checking conditions in the flowchart. When the overshoot is larger than 10% or the rising time is within 1ms, the iteration of K_p will be stopped with a fast control (1ms) and relatively low overshoot (10%). The design principle is to search an optimal combination of K_{ad} and K_p to achieve fast control performance without exciting too much oscillation. The influence of K_{ad} focuses more on the active damping which is reflected by the overshoot than the rising time. Thus, the checking condition for K_{ad} places more strict emphasis on overshoot than the rising time. On the other hand, the K_p is functioned more on the tracking speed which is reflected by the rising time. Thus, the checking condition for K_p places more strict emphasis on rising time than the overshoot. With the proposed control parameter design flowchart, the K_{ad} and K_p are optimized as 7.51e-3 and 10, respectively. Also, a comparison of bode plots between designed active damping LCL control system and conventional system without active damping is shown in Fig. 11. The resonance spike is attenuated with the designed active damping control system. Thus, the robustness of the control system is improved.

The merits and demerits of the active damping and PI parameters combined design method are introduced as follows. Firstly, for the merits of this combined method, by sweeping the active damping factor and PI control gain to derive an optimal combination, the dynamic performance and robustness during transient and ride through/trip periods are improved. Also, the issue of oscillation caused by variable frequency operation can be attenuated by the control design method. Secondly, for the demerits of the combined design method, one more sampling information of capacitor current is needed which will induce some extra sensor or computation cost.

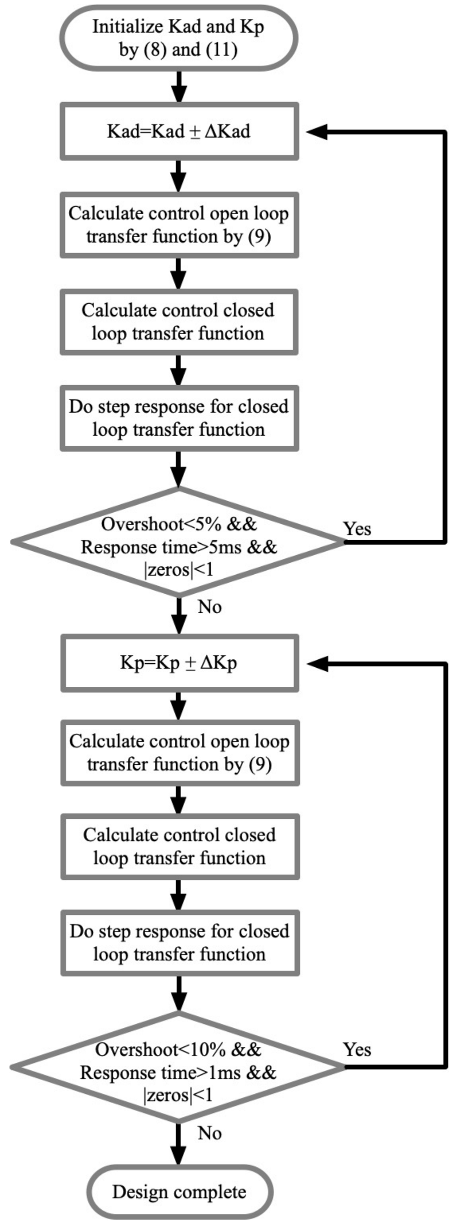

Fig. 9. The control parameter design flowchart.

V. RESULTS

The developed transformerless onboard EV charger is tested experimentally to validate the effectiveness of zero-sequence voltage control for the leakage current attenuation, VF-CSS for efficiency improvement and grid fault ride-through/trip capabilities. For the hardware specifications, C2M0025120D, Cree SiC MOSFET is applied for power switches and LAUNCHXL-F28379D is used for the controller. The power

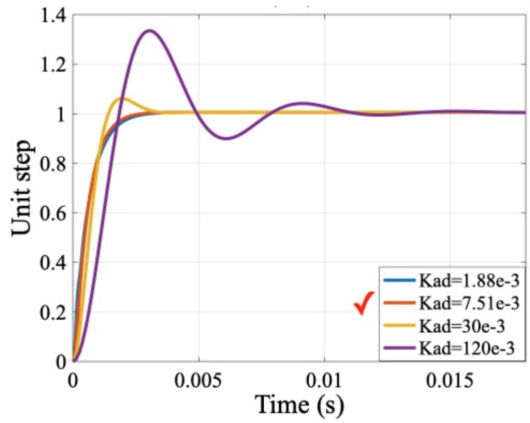

(a) Sweep the active damping gain.

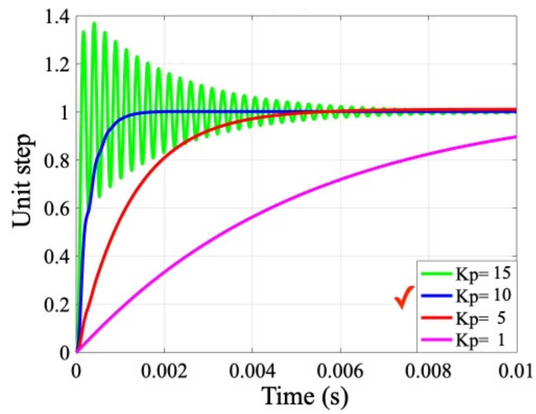

(b) Sweep the current control gain.

Fig. 10. The simulated step response of close loop control transfer function by sweeping (a) the active damping gain and (b) the current control gain.

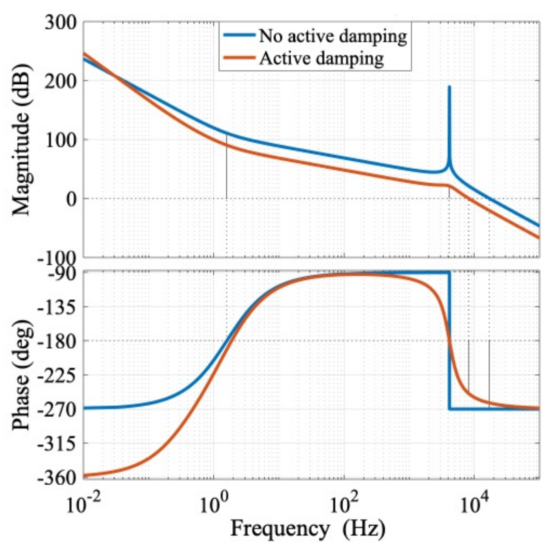

Fig. 11. The bode plots comparison between the designed active damping and without active damping control system.

PCB relay, T9SV1K15-12S, from TE Connectivity is leveraged for the transition between the grid and motor interfaces. The relays are controlled with a GPIO from the controller and can handle a rated current of 35A and rated voltage of 250VAC. Since the short pins of the relays are soldered to the PCB board, the power loss on the relays are low. For the electrical specifications, DC/AC converter is tested under battery side DC voltage of 700V-900V to grid side line-to-line AC voltage of 400V. The rated power is configured as 11-12kW. Variable switching frequency range is configured as 50kHz-160kHz. Switch side inductance, L_{fs}, is 45μH. Grid side inductance, L_{fg}, is 45μH. Output capacitance is 12μF. The testbench is shown in Fig. 12. The system parameter configurations are listed in table I.

A. *Zero Sequence Stabilization Test for Low Leakage Current*

The transformerless onboard EV charger is tested for the developed zero-sequence grid voltage control method and compared with the conventional method. Fig. 13 shows the grid voltage, leakage current, DC voltage and zero-sequence grid voltage waveforms with zero-sequence control. It is shown that the zero-sequence grid voltage has been stabilized at half of DC voltage. Also, for a detailed analysis of the developed zero sequence control method and modified three-phase topology, three cases are tested for comparison including: (1) the developed zero-sequence control method with modified circuit topology; (2) conventional control method with modified circuit topology; (3) conventional circuit topology without zero sequence control method. The corresponding leakage current and zero sequence voltage waveforms are shown in Fig. 14(a), 14(b) and 14(c), respectively. With the zero sequence control and modified topology, the leakage current is controlled within 20mA and the zero sequence voltage ripple is less than 10V. Without the zero sequence control applied to the modified topology, the leakage current is increased to be larger than 60mA and the zero sequence voltage ripple is larger than 60V. Finally, for the conventional topology without zero sequence voltage control, the leakage current is further increased to be larger than 1A. Thus, the modified topology can bypass some of the leakage current. And the zero sequence voltage control further attenuates the leakage current by a factor of 3.

TABLE I
SYSTEM PARAMETER CONFIGURATIONS

Parameter	Value
Grid voltage, $V_{grid,L-L}$	$400V_{L-L}$
Battery voltage, V_{batt}	700V-900V
Rated Power, P_N	11-12kW
Variable switching frequency	50kHz-160kHz
Switch side inductor, L_{fs}	45μH
Grid side inductor, L_{fg}	45μH
Output Capacitor, $C_{f,up/low}$	12μF
MOSFET	C2M0025120D
Controller	LAUNCHXL-F28379D
Efficiency @P_N	99.2%
Leakage current	15mA

B. Variable-Frequency Critical-Soft-Switching Test for High Efficiency

1) VF-CSS Performance: The full range AC current mode variable-frequency critical-soft-switching method is developed for the modified transformerless onboard EV charger with the frequency ranged from 50kHz to 160kHz. And the threshold current, I_{th}, is configured to be 2A for the peak/valley points of inductor current. As is shown in Fig. 15(b) and 15(c), different from 15(a) of the constant frequency hard switching, the three-phase inductor currents, $i_{L,abc}$, are all operating in critical soft switching mode at the full grid period range. The detailed drain-source voltage and current waveforms of the upper switch have been shown in Fig. 16. The ADC readings of the switching frequency and the corresponding inductor current in one phase are captured and plotted in Fig. 17 where the minimum frequency is applied at the top/bottom of the averaged inductor sine waveform and maximum frequency is applied at the zero crossing point of the averaged inductor sine waveform to achieve the boundary conditions of critical soft switching operation. The calculated switching frequency has followed equation (5). The high turn-on losses can be largely mitigated with VF-CSS. Thus, the efficiency is improved by 2% from from 97% to 99% as is shown in Fig. 18.

2) Thermal and Cooling Design: The thermal and cooling system design are illustrated in this section. Compared with the demonstrated soft switching operation mode, the conventional hard switching mode generates much more loss. The total loss is 88W at soft switching mode and 264W at hard switching mode. Thus, the cooling system is designed considering the worst case of hard switching. Under hard switching condition at the rated power level, the switching loss for each FET is 36.8W. The cooling module is designed based on the allowable temperature rising of the FET and the required thermal resistance of the heat sink. The thermal resistance can be derived as:

$$R_{TR} = \frac{T_j - T_{amb}}{P_{sw}} \tag{14}$$

where T_j, T_{amb}, P_{sw}, R_{th} and R_{in} are the junction temperature, ambient temperature, power dissipation and junction to case thermal resistance, respectively. Thus, assuming a maximum temperature rising of 75°C for C2M0025120D FET, the required thermal resistance for each phase is at least 1.14 K/°C. After the comprehensive consideration of compactness, air volume and speed, we leveraged the aluminum heatsink combined with axial fan, LAM/3/50/12, from FISCHER ELEKTRONIK to dissipate the heat from the FET. Each of the LAM/3/50/12 module is responsible for one phase of upper/lower switches. And the LAM/3/50/12 module has a thermal resistance of 1.94 K/°C which satisfies the thermal requirement. The thermal performance of FET has been shown in Fig. 19 where the temperature rising is within the expected design range.

3) Merits and Demerits of VF-CSS: For the merits of variable-frequency critical-soft-switching, firstly, the switching losses are reduced. Based on the datasheet of Cree SiC MOSFET, C2M0025120D, the turn-on loss is 4 times larger than the turn-off loss. Thus, the implementation of soft-switching turn-on for both upper and lower switches saves switching losses which contributes to an improvement of efficiency by more than 2% for the designed onboard charger. Secondly, the power density of the charger can be increased by reducing the inductance. For the purpose of soft switching, a large current ripple is required which means the inductor size is reduced. This characteristic of VF-CSS enables an increase of switching frequency by a factor of 5 and the reduction of inductance by 20 times. For the demerits of VF-CSS, firstly, the transient performance could be deteriorated since the switching frequency is time-varying. The variable frequency may cause some oscillation during the transient that would bring extra challenges on a robust control design. Secondly, the variable PWM signals for switching may cause a mismatch between the sampling frequency and switching frequency. Especially when the large ripple inductor current is required to be sampled for soft switching, the mismatch may cause big offset and sampling error.

C. Transient Behavior of Grid Voltage/Frequency Fault Ride-Through/Trip Test

The transient performance based on the control parameter design is shown in Fig. 20. Specifically, the experimental ADC readings of current steps from 2A to 6A and 6A to 2A are plotted in Fig. 20(a) and 20(b), respectively. Also, the experimental waveforms of grid current/voltage with a current step of 4A are validated and shown in Fig. 21 with control gain swept from 5 to 15. The optimal rising time and overshoot performances are achieved with the control gain of 10 to deliver robust grid voltage/frequency fault ride through/trip behaviors.

Fig. 22(a) to Fig. 22(e) show the inductor current, grid voltage, grid current, DC voltage waveforms under different grid voltage abnormal conditions. Specifically, in Fig. 22(a) from $106\%V_N$ to $115\%V_N$, the charger can ride through for 1s and then trip. In Fig. 22(b) from $106\%V_N$ to $125\%V_N$, the charger can trip immediately during transient. In Fig. 22(c) from $95\%V_N$ to $80\%V_N$, the charger can ride through for 2s and then trip. In Fig. 22(d) from $95\%V_N$ to $60\%V_N$, the charger can ride through for 0.32s and then trip. In Fig. 22(e) from $95\%V_N$ to $25\%V_N$, the charger can trip immediately during transient.

Fig. 23(a) and Fig. 23(b) show the inductor current, grid voltage, grid current, DC voltage waveforms under different grid frequency abnormal conditions. Specifically, in Fig. 23(a) from 51.5Hz to 52.5Hz and Fig. 23(b) from 48Hz to 46.5Hz, the charger can trip immediately based on a rated grid frequency of 50Hz.

D. Comparative Analysis for the Charger Design

A comparative analysis between the developed onboard charger and the existing designs is summarized in the aspects of efficiency, power density and grid-interfaced functions. Firstly, for the efficiency, the designs in [25], [29], [32], [34] and [31] achieved the efficiency range from 90% to 95% while [26] reached a peak efficiency of 98%. The proposed design achieves above 99% due to the VF-CSS and transformerless topology. Secondly, for the power density, [25] measured

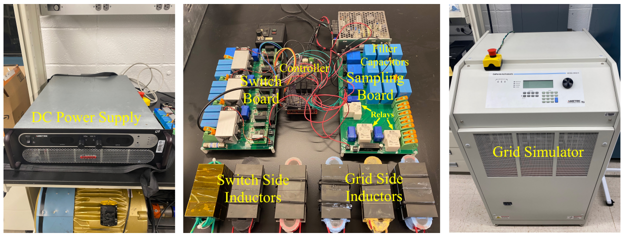

Fig. 12. The testbench of the developed non-isolated onboard EV charger.

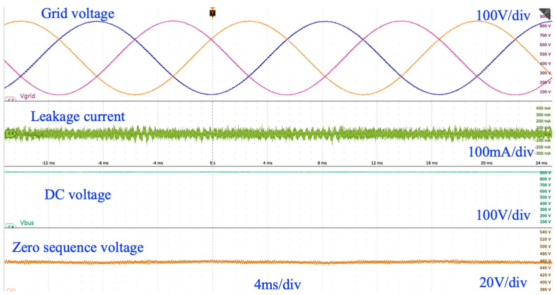

Fig. 13. The experimental grid voltage, leakage current, DC voltage and zero-sequence grid voltage waveforms with the modified non-isolated topology and control method.

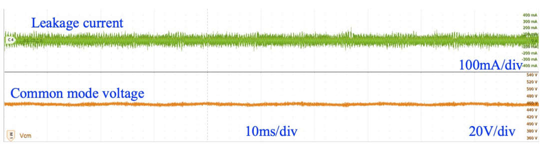

(a) Modified topology with zero-sequence voltage control.

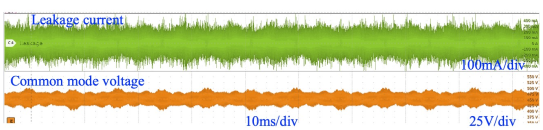

(b) Modified topology without zero-sequence voltage control.

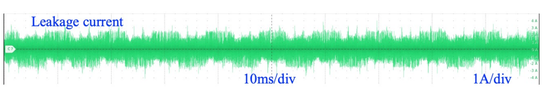

(c) Traditional topology without zero-sequence voltage control.

Fig. 14. The experimental comparison of leakage current and common mode voltage (a) for the modified topology with zero-sequence voltage control (b) for the modified topology without zero-sequence voltage control and (c) for the traditional topology without zero-sequence voltage control.

0.55kW/L in the prototype. The proposed design in this paper achieves 9kW/L which is 2 and 2.5 times higher than the US DOE 2020 and 2025 targets for the onboard charger, respectively [41]. Finally, for the grid-interfaced functions, [27], [28], [30] designed Vehicle-to-Grid (V2G) functions to regulate the grid voltage fluctuation by providing reactive power compensation. However, when abnormal grid conditions occur, the robust control design lacks research. This paper provides the ride through/trip control design for harsher grid environment.

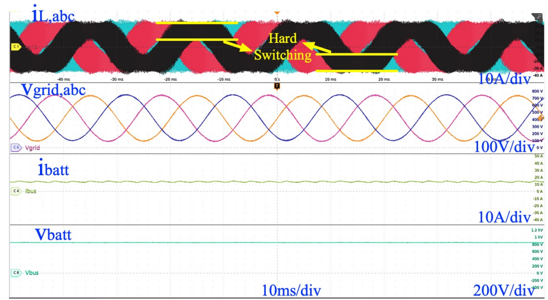

(a) Hard switching waveforms.

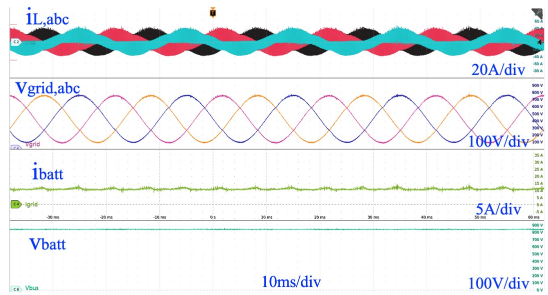

(b) VF-CSS waveforms.

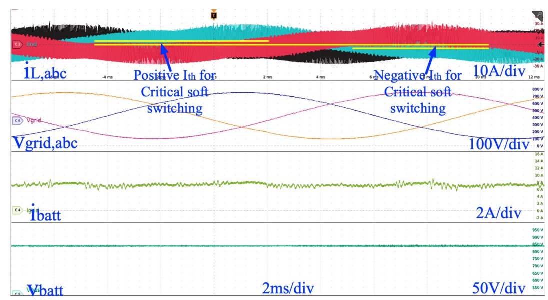

(c) Zoomed VF-CSS waveforms.

Fig. 15. Experimental results of (a) hard switching (b) variable-frequency critical-soft-switching waveforms of inductor current, grid voltage, battery current and battery voltage and (c) zoomed waveforms.

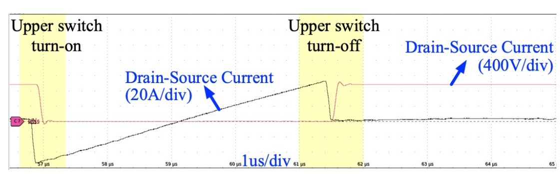

Fig. 16. The drain-source voltage and current experimental waveforms for the upper switch.

VI. Conclusion

A transformerless EV onboard charger is designed with zero sequence voltage stabilized control method, AC current mode full range variable-frequency critical-soft-switching, optimal control parameter design procedure based on active damping and grid fault ride through/trip strategies under grid voltage/frequency abnormal conditions. The topological modification of connecting the common points of three-phase

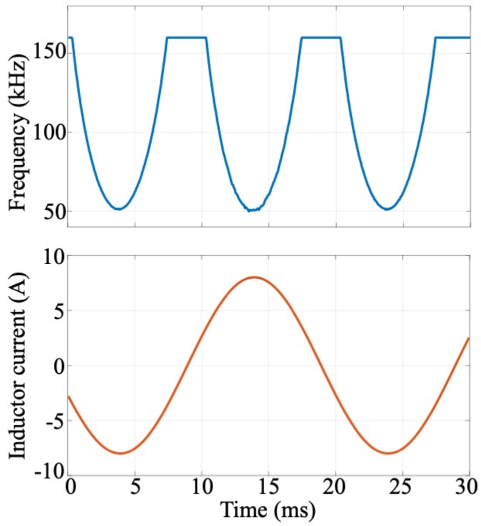

Fig. 17. Experimentally collected data of variable-frequency critical-soft-switching ADC readings of switching frequency and inductor current.

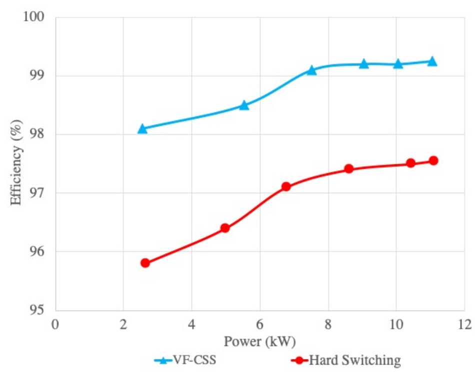

Fig. 18. Efficiency curve of the transformerless onboard EV charger with variable-frequency critical-soft-switching derived from experiments.

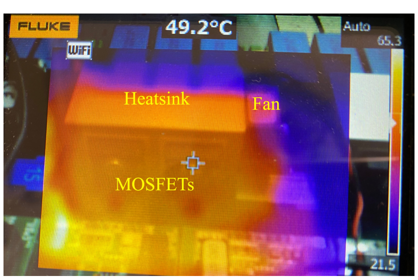

Fig. 19. Thermal performance of the designed cooling system.

output capacitors and the positive/negative DC bus terminals contributes to the reduction of leakage current with the zero sequence voltage controller. The full range AC current mode variable-frequency critical-soft-switching technique improves the efficiency to be higher than 99%. The active damping based optimal control parameter design improves the dynamic performance which contributes to the ride-through/trip capabilities of the charger. The grid standard requirements of IEEE Std. 1547 are satisfied based on the proposed optimal control parameter tuning and ride-through/trip design. Different grid

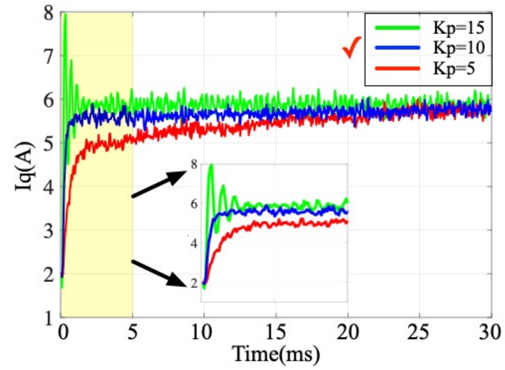

(a) Current step from 2A to 6A.

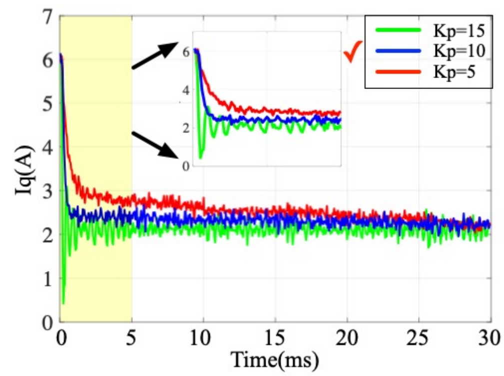

(b) Current step from 6A to 2A.

Fig. 20. The experimental ADC readings of current steps from (a) 2A to 6A and (b) 6A to 2A with different control gains from 5, 10 to 15.

voltage/frequency abnormal condition cases, leakage current performance and full ranged AC current mode variable-frequency critical-soft-switching operations have been tested experimentally to verify the design.

REFERENCES

[1] S. Wang, H. Li, Z. Zhang, M. Li, J. Zhang, X. Ren, and Q. Chen, "Multi-function Capability of SiC Bidirectional Portable Chargers for Electric Vehicles," *IEEE Journal of Emerging and Selected Topics in Power Electronics*, vol. 6777, no. c, 2021.

[2] C. Jiang, B. Lei, H. Teng, and H. K. Bai, "The power-loss analysis and efficiency maximization of a silicon-carbide MOSFET based three-phase 10kW bi-directional EV charger using variable-DC-bus control," *ECCE 2016 - IEEE Energy Conversion Congress and Exposition, Proceedings*, vol. 4, no. 3, pp. 880–892, 2016.

[3] C. Shi and A. Khaligh, "A Two-Stage Three-Phase Integrated Charger for Electric Vehicles with Dual Cascaded Control Strategy," *IEEE Journal of Emerging and Selected Topics in Power Electronics*, vol. 6, no. 2, pp. 898–909, 2018.

[4] D. H. Kim, M. J. Kim, and B. K. Lee, "An integrated battery charger with high power density and efficiency for electric vehicles," *IEEE Transactions on Power Electronics*, vol. 32, no. 6, pp. 4553–4565, 2017.

[5] H. Tu, H. Feng, S. Srdic, and S. Lukic, "Extreme Fast Charging of Electric Vehicles: A Technology Overview," *IEEE Transactions on Transportation Electrification*, vol. 5, no. 4, pp. 861–878, 2019.

[6] H. Jafari, M. Moghaddami, T. O. Olowu, A. Sarwat, and M. Mahmoudi, "Virtual Inertia-Based Multi-Power Level Controller for Inductive Electric Vehicle Charging Systems," *IEEE Journal of Emerging and Selected Topics in Power Electronics*, vol. 6777, no. 1541108, pp. 1–1, 2020.

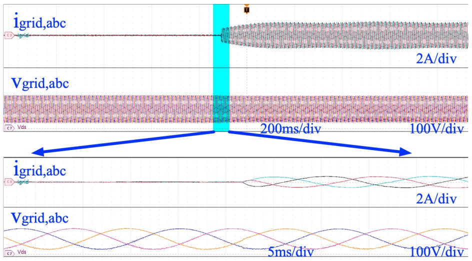

(a) K_p gain of 5.

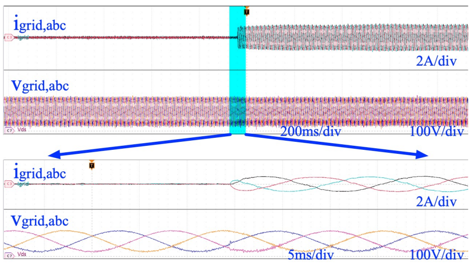

(b) K_p gain of 10.

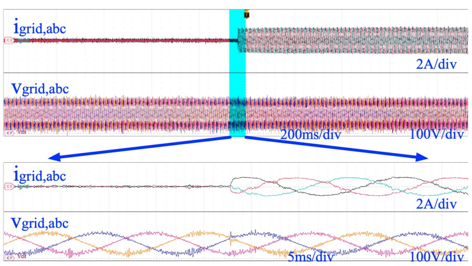

(c) K_p gain of 15.

Fig. 21. The experimental grid current/voltage waveforms with a current step of 4A at K_p gain of (a) 5 (b) 10 and (c) 15.

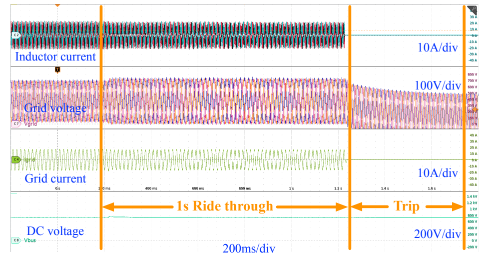

(a) $106\%V_N$ to $115\%V_N$.

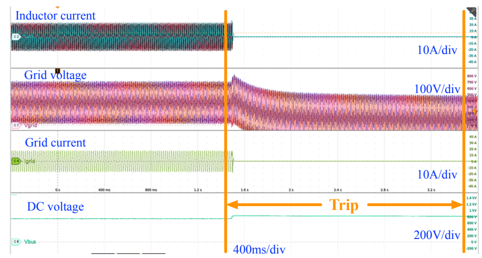

(b) $106\%V_N$ to $125\%V_N$.

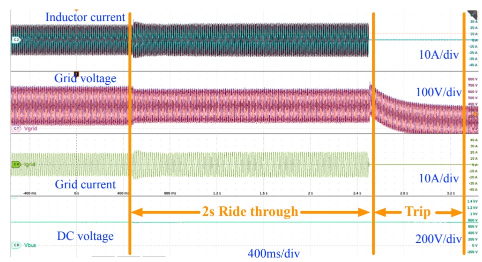

(c) $95\%V_N$ to $80\%V_N$.

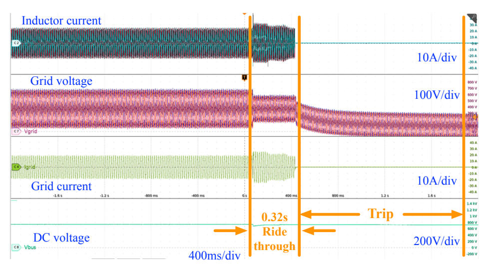

(d) $95\%V_N$ to $60\%V_N$.

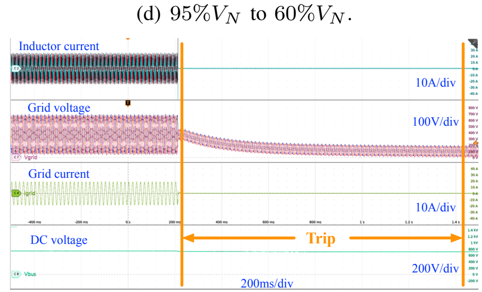

(e) $95\%V_N$ to $25\%V_N$.

Fig. 22. Experimental results of ride-through and trip waveforms of the developed transformerless onboard EV charger under grid voltage abnormal conditions.

[7] H. Tanaka, F. Ikeda, T. Tanaka, H. Yamada, and M. Okamoto, "Novel Reactive Power Control Strategy Based on Constant DC-Capacitor Voltage Control for Reducing the Capacity of Smart Charger for Electric Vehicles on Single-Phase Three-Wire Distribution Feeders," *IEEE Journal of Emerging and Selected Topics in Power Electronics*, vol. 4, no. 2, pp. 481–488, 2016.

[8] L. Zhou, F. Gao, and T. Xu, "A Family of Neutral-Point-Clamped Circuits of Single-Phase PV Inverters: Generalized Principle and Implementation," *IEEE Transactions on Power Electronics*, vol. 32, no. 6, pp. 4307–4319, 2017.

[9] Ó. López, F. D. Freijedo, A. G. Yepes, P. Fernández-Comesaña, J. Malvar, J. Doval-Gandoy, and R. Teodorescu, "Eliminating ground current in a transformerless photovoltaic application," *IEEE Transactions on Energy Conversion*, vol. 25, no. 1, pp. 140–147, 2010.

[10] Y. Du, X. Zhou, S. Bai, S. Lukic, and A. Huang, "Review of non-isolated bi-directional DC-DC converters for plug-in hybrid electric vehicle charge station application at municipal parking decks," *Conference Proceedings - IEEE Applied Power Electronics Conference and Exposition - APEC*, no. 1, pp. 1145–1151, 2010.

[11] B. Yang, W. Li, Y. Gu, W. Cui, and X. He, "Improved transformerless inverter with common-mode leakage current elimination for a photovoltaic grid-connected power system," *IEEE Transactions on Power Electronics*, vol. 27, no. 2, pp. 752–762, 2012.

[12] F. Chen, R. Burgos, and D. Boroyevich, "A Bidirectional High-Efficiency Transformerless Converter with Common-Mode Decoupling for the Interconnection of AC and DC Grids," *IEEE Transactions on Power Electronics*, vol. 34, no. 2, pp. 1317–1333, 2019.

[13] L. Zhou, F. Gao, and T. Xu, "Implementation of Active NPC Circuits in Transformer-Less Single-Phase Inverter With Low Leakage Current,"

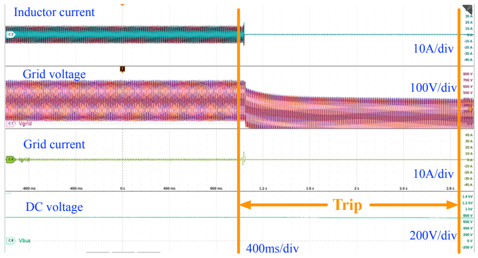

(a) 61.5Hz to 62.5Hz.

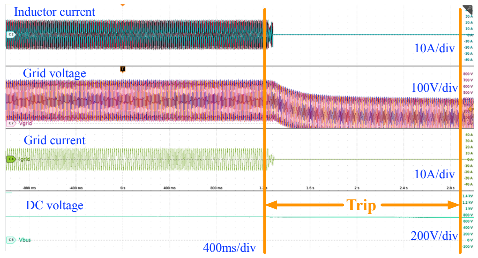

(b) 58Hz to 56.5Hz.

Fig. 23. Experimental trip waveforms of the developed transformerless onboard EV charger under grid frequency abnormal conditions.

IEEE Transactions on Industry Applications, vol. 53, no. 6, pp. 5658–5667, 2017.

[14] L. Zhou, M. Eull, W. Wang, G. Cen, and M. Preindl, "Design of transformerless electric vehicle charger with symmetric ac and dc interfaces," in *2021 IEEE Applied Power Electronics Conference and Exposition (APEC)*. IEEE, 2021, pp. 2769–2774.

[15] S. Moury and J. Lam, "A Soft-Switched Power Module with Integrated Battery Interface for Photovoltaic-Battery Power Architecture," *IEEE Journal of Emerging and Selected Topics in Power Electronics*, vol. 8, no. 3, pp. 3090–3110, 2020.

[16] M. Pahlevani and P. K. Jain, "Soft-Switching Power Electronics Technology for Electric Vehicles: A Technology Review," *IEEE Journal of Emerging and Selected Topics in Industrial Electronics*, vol. 1, no. 1, pp. 80–90, 2020.

[17] Y. Wang, H. Song, and D. Xu, "Soft-Switching Bidirectional DC/DC Converter with an LCLC Resonant Circuit," *IEEE Journal of Emerging and Selected Topics in Power Electronics*, vol. 7, no. 2, pp. 851–864, 2019.

[18] B. Akhlaghi and H. Farzanehfard, "Soft Switching Interleaved High Step-Up Converter With Multifunction Coupled Inductors," *IEEE Journal of Emerging and Selected Topics in Industrial Electronics*, vol. 2, no. 1, pp. 13–20, 2020.

[19] R. H. Ashique and Z. Salam, "A Family of True Zero Voltage Zero Current Switching (ZVZCS) Nonisolated Bidirectional DC-DC Converter with Wide Soft Switching Range," *IEEE Transactions on Industrial Electronics*, vol. 64, no. 7, pp. 5416–5427, 2017.

[20] M. Mohammadi, E. Adib, and M. R. Yazdani, "Family of soft-switching single-switch PWM converters with lossless passive snubber," *IEEE Transactions on Industrial Electronics*, vol. 62, no. 6, pp. 3473–3481, 2015.

[21] M. Mirhosseini, J. Pou, and V. G. Agelidis, "Single- and Two-Stage Inverter-Based Grid-Connected Photovoltaic Power Plants With Ride-Through Capability Under Grid Faults," *IEEE Transactions on Sustainable Energy*, vol. 6, no. 3, pp. 1150–1159, 2015.

[22] P. H. Huang, M. S. El Moursi, and S. A. Hasen, "Novel Fault Ride-Through Scheme and Control Strategy for Doubly Fed Induction Generator-Based Wind Turbine," *IEEE Transactions on Energy Conversion*, vol. 30, no. 2, pp. 635–645, 2015.

[23] A. Merabet, L. Labib, and A. M. Ghias, "Robust model predictive control for photovoltaic inverter system with grid fault ride-through capability," *IEEE Transactions on Smart Grid*, vol. 9, no. 6, pp. 5699–5709, 2018.

[24] L. Zhu, H. Bai, A. Brown, and M. McAmmond, "Transient analysis when applying gan + si hybrid switching modules to a zero-voltage-switching ev onboard charger," *IEEE Transactions on Transportation Electrification*, vol. 6, no. 1, pp. 146–157, 2020.

[25] S. Li, J. Deng, and C. C. Mi, "Single-stage resonant battery charger with inherent power factor correction for electric vehicles," *IEEE Transactions on Vehicular Technology*, vol. 62, no. 9, pp. 4336–4344, 2013.

[26] J. Deng, S. Li, S. Hu, C. C. Mi, and R. Ma, "Design methodology of llc resonant converters for electric vehicle battery chargers," *IEEE Transactions on Vehicular Technology*, vol. 63, no. 4, pp. 1581–1592, 2014.

[27] J. A. Suul, S. D'Arco, and G. Guidi, "Virtual synchronous machine-based control of a single-phase bi-directional battery charger for providing vehicle-to-grid services," *IEEE Transactions on Industry Applications*, vol. 52, no. 4, pp. 3234–3244, 2016.

[28] Q. Hu, S. Bu, and V. Terzija, "A distributed p and q provision-based voltage regulation scheme by incentivized ev fleet charging for resistive distribution networks," *IEEE Transactions on Transportation Electrification*, vol. 7, no. 4, pp. 2376–2389, 2021.

[29] X. Liu, F. Yu, J. Mao, and H. Yang, "Pre- and post-fault operations of six-phase electric-drive-reconstructed onboard charger for electric vehicles," *IEEE Transactions on Transportation Electrification*, pp. 1–1, 2021.

[30] D. B. Wickramasinghe Abeywardana, P. Acuna, B. Hredzak, R. P. Aguilera, and V. G. Agelidis, "Single-phase boost inverter-based electric vehicle charger with integrated vehicle to grid reactive power compensation," *IEEE Transactions on Power Electronics*, vol. 33, no. 4, pp. 3462–3471, 2018.

[31] Y. Zhang, J. Fang, F. Gao, S. Gao, D. J. Rogers, and X. Zhu, "Integrated high- and low-frequency current ripple suppressions in a single-phase onboard charger for evs," *IEEE Transactions on Power Electronics*, vol. 36, no. 2, pp. 1717–1729, 2021.

[32] S. Kim and F.-S. Kang, "Multifunctional onboard battery charger for plug-in electric vehicles," *IEEE Transactions on Industrial Electronics*, vol. 62, no. 6, pp. 3460–3472, 2015.

[33] H. J. Raherimihaja, Q. Zhang, T. Na, M. Shao, and J. Wang, "A three-phase integrated battery charger for evs based on six-phase open-end winding machine," *IEEE Transactions on Power Electronics*, vol. 35, no. 11, pp. 12 122–12 132, 2020.

[34] S. Ranjith, V. Vidya, and R. S. Kaarthik, "An integrated ev battery charger with retrofit capability," *IEEE Transactions on Transportation Electrification*, vol. 6, no. 3, pp. 985–994, 2020.

[35] IEEE Standard Association, *IEEE Std. 1547-2018. Standard for Interconnection and Interoperability of Distributed Energy Resources with Associated Electric Power Systems Interfaces*, 2018.

[36] M. B. Meier, D. S. S. Avelino, A. A. Badin, E. F. R. Romaneli, and R. Gules, "Soft-switching high static gain DC-DC converter without auxiliary switches," *IEEE Transactions on Industrial Electronics*, vol. 65, no. 3, pp. 2335–2345, 2018.

[37] F. Ahmadi, E. Adib, and M. Azari, "Soft switching bidirectional converter for reflex charger with minimum switches," *IEEE Transactions on Industrial Electronics*, vol. 67, no. 10, pp. 8355–8362, 2020.

[38] C. Wessels, F. Gebhardt, and F. W. Fuchs, "Fault ride-through of a DFIG wind turbine using a dynamic voltage restorer during symmetrical and asymmetrical grid faults," *IEEE Transactions on Power Electronics*, vol. 26, no. 3, pp. 807–815, 2011.

[39] S. F. Zarei, H. Mokhtari, M. A. Ghasemi, and F. Blaabjerg, "Reinforcing Fault Ride through Capability of Grid Forming Voltage Source Converters Using an Enhanced Voltage Control Scheme," *IEEE Transactions on Power Delivery*, vol. 34, no. 5, pp. 1827–1842, 2019.

[40] R. Peña-Alzola, M. Liserre, F. Blaabjerg, M. Ordonez, and Y. Yang, "LCL-filter design for robust active damping in grid-connected converters," *IEEE Transactions on Industrial Informatics*, vol. 10, no. 4, pp. 2192–2203, 2014.

[41] "US DRIVE Electrical and Electronics Technical Team Roadmap," United States Department of Energy, Tech. Rep. October, 2017. [Online]. Available: https://www.energy.gov/sites/prod/files/2017/11/f39/EETT Roadmap 10-27-17.pdf

Liwei Zhou (S'15) received the B.E. and the M.E., both in Electrical Engineering, from Shandong University, Jinan, China in 2014 and 2017, respectively. He is currently working toward the Ph.D. degree in Motor Drives and Power Electronics Laboratory (MPLab), Columbia University, New York City, NY, USA. Since 2017, he has been a Graduate Research Assistant with MPLab. His current research interests include soft-switching techniques for modular power converter, model predictive control and other advanced control technologies, grid-connected converter and EV battery charging control, inductor design. He received the IEEE Energy Conversion Congress & Expo, 2018 Student Travel Award. He is also the co-recipient of the Best Student Paper Award of the IEEE Transportation Electrification Conference and Expo (ITEC), 2021.

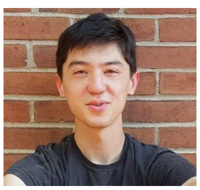

Matthew Jahnes (S'20) received the B.S. degree in electrical engineering from Rensselaer Polytechnic Institute in Troy, NY in 2017 and the M.S. degree in electrical engineering from Columbia University in New York, NY in 2019. He is currently working towards his Ph.D. at the Motor Drives and Power Electronics Laboratory (MPLab), Columbia University, New York, NY. His current research interests include novel power conversion topologies and high efficiency/high power density converter design.

Matthias Preindl (S'12-M'15-SM'18) received the B.Sc. degree in electrical engineering (*summa cum laude*) from the University of Padua, Italy, the M.Sc. degree in electrical engineering and information technology from ETH Zurich, Switzerland, and the Ph.D. degree in energy engineering from the University of Padua, in 2008, 2010, and 2014, respectively. He is currently Associate Professor of Power Electronic Systems in the Department of Electrical Engineering at Columbia University, USA. Prior to joining Columbia University in 2016, he was an R&D Engineer of Power Electronics and Drives at Leitwind AG, Italy (2010-2012), a Post Doctoral Research Associate with the McMaster Institute for Automotive Research and Technology, McMaster University, Hamilton, ON, Canada (2014-2015), and a Sessional Professor in the Department of Electrical and Computer Engineering, McMaster University (2015). He serves as the area editor of vehicular electronics and systems at the IEEE Transactions on Vehicular Technology and as the general chair of the 2022 IEEE/AIAA ITEC+EATS. He received several awards and honors including the Horiba Awards Honorable Mention (Japan, 2019), the Futura Foundation Award (Italy, 2017), the NSF CAREER Award (USA, 2017), and he is the co-recipient of several best paper and presentation recognitions including the 2019 IEEE Transactions on Industrial Electronics best paper award.